# An Algorithm for Automated Separation of Trabecular Bone from Variably Thick Cortices in High-Resolution Computed Tomography Data

Ida C. Ang, Maria Fox, John D. Polk, and Mariana E. Kersh\*

Abstract—Objective: Structural measurements after separation of cortical from trabecular bone are of interest to a wide variety of communities but are difficult to obtain because of the lack of accurate automated techniques. Methods: We d present a structure-based algorithm for separating cortical from trabecular bone in binarized images. Using the thickness of the cortex as a seed value, bone connected to the cortex within a spatially local threshold value is identified and separated from the remaining bone. The algorithm was tested on seven biological data sets from four species imaged using micro-computed tomography ( $\mu$ -CT) and high-resolution peripheral quantitative computed tomography (HR-pQCT). Area and local thickness measurements were compared to images segmented manually. Results: The algorithm was approximately 11 times faster than manual measurements and the median error in cortical area was  $-4.47 \pm 4.15\%$ . The median error in cortical thickness was approximately 0.5 voxels for  $\mu$ -CT data and less than 0.05 voxels for HR-pQCT images resulting in an overall difference of -28.1  $\pm$ 71.1 µm. Conclusion: A simple and readily implementable methodology has been developed that is repeatable, efficient, and requires few user inputs, providing an unbiased means of separating cortical from trabecular bone. Significance: Automating the segmentation of variably thick cortices will allow for the evaluation of large data sets in a time-efficient manner and allow for full-field analyses that have been previously limited to small regions of interest. The MATLAB code can be downloaded from https://github.com/TBL-UIUC/downloads.git.

Index Terms—Bone, Cortical, Feature extraction, Highresolution imaging, Image analysis, Image processing, Image segmentation, MATLAB, Morphological operations

Manuscript Received Sept 5, 2018; Revised Jan 6, 2019 and May 6, 2019; accepted June 10, 2019. Funding for this study was provided by the U.S. National Science Foundation BCS-1638756, The Leakey Foundation, and the University of Illinois Research Board. Funding for the presentation of preliminary results at the Orthopaedic Research Society annual conference was provided by the University of Illinois Office of Undergraduate Research.

I.C. Ang was with the Department of Bioengineering at the University of Illinois at Urbana-Champaign, Urbana, IL, USA. She is now with the department of Mechanical Engineering at Cornell University, Ithaca, NY, USA.

M. Fox is with the Department of Anthropology at the University of Illinois at Urbana-Champaign, Urbana, IL, USA.

J.D. Fox is with Department of Anthropology and the Department of Surgery at the University of Illinois at Urbana-Champaign, Urbana, IL, USA.

\*M.E. Kersh is with the Department of Mechanical Science and Engineering and the Beckman Institute for Advanced Science and Technology at the University of Illinois at Urbana-Champaign, Urbana, IL, USA (correspondence email: mkersh@illinois.edu).

#### I. INTRODUCTION

Micro-computed tomography ( $\mu$ -CT) and high-resolution peripheral quantitative computed tomography (HR-pQCT) are primary sources of structure and composition information for analyses of bone properties [1]. The increase in  $\mu$ -CT availability and capacity, coupled with increased computational resources in research and clinical settings, has allowed for both cross-sectional and longitudinal studies to evaluate spatially local changes in bone under a variety of conditions. The (re)modeling response of bone to mechanical loading has been a longstanding subject of interest and has applications spanning from anthropology to medicine [1-8].

Whereas the analysis of diaphyseal cortical properties are relatively straightforward, analyses of the epiphyses of bone remain challenging because of the simultaneous hierarchical and heterogeneous structure of bone. A rigorous assessment of cortical and trabecular properties requires separating these regions for independent analyses. However, quantifying cortical bone parameters is difficult in regions where the trabecular mesh is highly complex and closely connected to the outer shell of bone. Obtaining accurate bone parameters is especially problematic in the epiphyses of bone, where subchondral bone, the thin layer of cortical bone underlying the joint articular cartilage, is much thinner than bone at the diaphysis [9], [10].

To avoid misidentifying subchondral bone as trabecular bone, volumes of interest (VOI) at the center of the joint geometry have been used [11-14]. However, bone functional signals may be lost within this central region, and the clearest signal is likely to be present close to the joint surface [6], [15]. Accounting for the spatial variation in micro-structure throughout the entire bone, in contrast to single isolated VOI-based analyses, may be a critical determinant for understanding how bone adapts to changes in mechanical loading.

The use of different segmentation schemes based on global, local, or adaptive threshold values has been widely discussed in the literature and the reader is referred to Li et al. [16] and Wong and Manske [17] for a review of algorithms used to

binarize images. While there have been significant advances in cortical bone binarization algorithms for  $\mu$ -CT and HR-pQCT, the methods needed to analyze the resulting image stacks require further development. The separation of bone for cortical-only analyses requires the capacity to clearly distinguish the two structures. Several algorithms of varying complexity have been proposed to separate the cortex from the trabecular structure with many relying on a combination of threshold-based techniques combined with morphological opening/closing or erosion/dilation operations. The amount of bone to open/close or erode/dilate is determined by a kernel or structuring element size, which may be determined iteratively or via average trabecular thickness in the region of interest [18]. Work by Buie et al. (refined later by Burghardt et al.) showed that a small set of dual-threshold values could be used to reliably segment cortical bone in a variety of samples at different  $\mu$ -CT resolutions [19], [20]. For HR-pQCT, Valentinitsch et al. developed a threshold-independent segmentation tool (TIST) which utilized machine learning schemes to segment cortical bone [21].

Other methods for identifying cortical boundaries include profiling of the Hounsfield unit (HU) values along a line passing through the cortex [22]. Others have proposed using the normal vectors from an outer contour, again based on a threshold unit, in combination with morphological operations using kernel sizes derived from the trabecular structure to minimize artificial changes in structure [18, 23, 24]. However, variation due to scanner drift, image noise, and partial volume effects complicate the identification of a mean HU value or thresholds for segmentation and the value would have to be periodically tuned for optimal results.

Here we present an automated two-dimensional (2D) approach that takes advantage of structural information within a binarized image to identify the cortical-trabecular border rather than a threshold or HU based approach. Furthermore, the implementation of the algorithm can be accomplished with commonly available research tools, ImageJ (BoneJ plug-in) [25] and MATLAB (Version R2019a MathWorks, Natick, MA, USA). Preliminary cortical thickness results utilizing the algorithm have been reported [26].

#### II. METHODS

## A. Image Input Requirements

Two input datasets are required: 1. a binary image (Fig. 1A) and 2. a thickness map of the structures within the image (Fig. 1C). The ImageJ plug-in, BoneJ, calculates a thickness map by defining the thickness as the greatest sphere that can fit within the input image structure [25]. Using BoneJ, thickness maps can be calculated from binarized image sets and imported into the MATLAB algorithm as matrices. If there is no thickness value within a pixel, the algorithm assigns these pixels zero.

# B. Image Border Detection

Similar to Buie et. al. [19], we initially assume that the cortical shell of bone exists as a continuous surface in order to create an external boundary for evaluating cortical thickness.

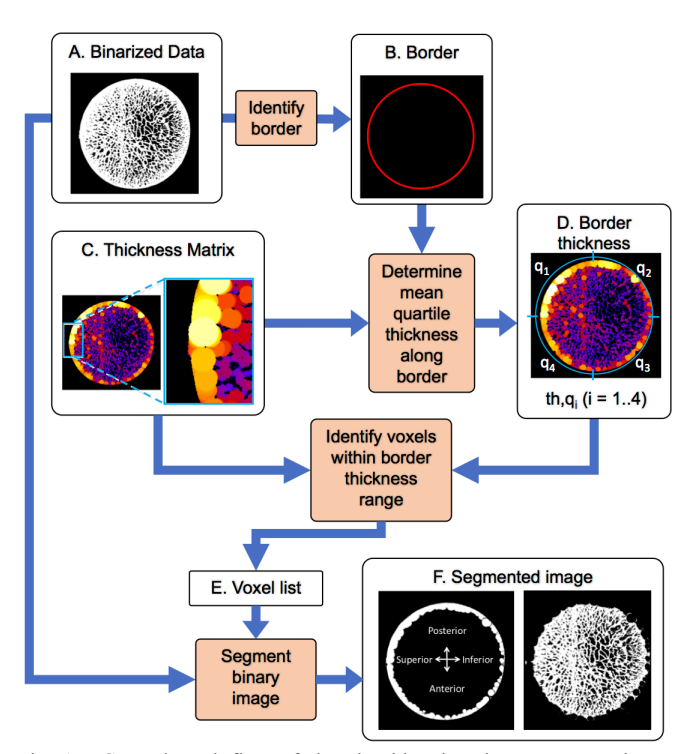


Fig. 1. General work-flow of the algorithm based on two user inputs, binarized data and thickness matrix obtained from ImageJ plugin, BoneJ. Example images from the human femoral head.

Note that this boundary may also include "zero" values based on the thickness map; however, it is common to have regions of cortical bone that are as thin as the surrounding trabecular bone or are undetectable in the initial segmentation due to image noise or partial volume effects. Similarly, gaps in cortical bone may exist in pathological specimens (e.g., osteoporotic bone) or specimens from museum collections. These image artifacts may result in errors in the detection of a continuous border.

Therefore, we implemented an initial border check to ensure that a continuous border exists within the image by estimating a maximum border length and comparing it to the border within the image. The maximum border length was calculated using the extrema points of the binarized image to calculate the maximum distance from top to bottom,  $X_{\rm est}$ , and from right to left,  $Y_{\rm est}$ , (Fig. 2). The extrema points are connected to form triangles enclosing rough quadrants of the object border. This evaluation of the border is based on the assumption that the external contour of bone is convex or concave, not undulating; therefore, the summation of the opposite and adjacent sides of the triangle will always be larger than the border. These maximum distances were used to calculate a maximum perimeter,  $B_e$ , using (1).

$$B_e = 2(X_{\text{est}} + Y_{\text{est}}) \tag{1}$$

The maximum rectangular perimeter value,  $B_e$ , were compared to the initial calculation of the external border using MATLAB (function *bwboundaries*). If the border length is larger than the rectangular estimate, a warning is issued that the border should be corrected to fill gaps or holes that

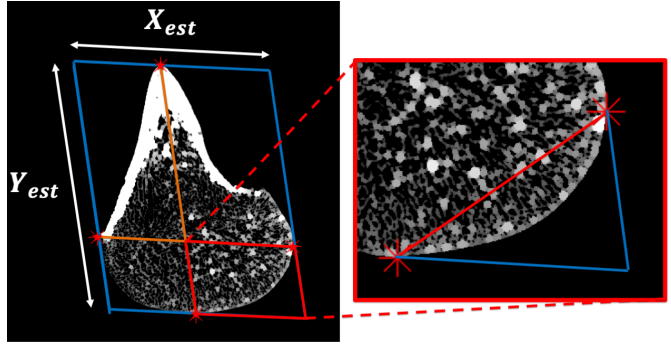


Fig. 2. Rectangular estimation of the border,  $B_{\rm e}$ , calculated from extrema points for the lateral condyle of a chimpanzee. The maximum distances in each direction is denoted by  $X_{\rm est}$  and  $Y_{\rm est}$ .

typically cause an overestimation of the border. These can be corrected using morphological erosion and dilation operations or other corrective options available within image processing software packages.

## C. Thickness-Based Separation

The thickness matrix, determined with BoneJ, was used to extract regions connected to the outer border that are of similar local thickness values. The thickness for any given pixel, p, along the boundary, th<sub>p</sub>, of bone was identified from the thickness matrix (Fig. 1C). The bone border was then sectioned into quadrants (Fig. 1D), and the average of all nonzero thickness values at each quadrant was calculated, th<sub>q</sub>. The average quadrant thickness, th<sub>q</sub>, containing the pixel of interest was then used to determine the range of thickness values to include in the segmentation (2).

Next, a subset of pixels,  $p_s$ , to evaluate was identified by centering a window equal to 10% of the image width and length around the pixel of interest. Within this window, half of the global minimum thickness (th<sub>min</sub>) value of each quadrants average thickness value was used as an upper and lower threshold to identify pixels of similar local thickness to the pixel of interest according to (2).

$$p_{ss} \; = \; (th_p - \frac{th_{min}}{2} \times th_q) < p_s < (th_p + \frac{th_{min}}{2} \times th_q) \quad (2)$$

where  $p_{ss}$  is the total subset of pixels,  $p_s$ , within the range associated with the pixel on the border,  $th_p$ , and  $p_{min}$  is the global minimum thickness value.

This process was then repeated for every th<sub>p</sub>, continuing clockwise to the next location, i+1, along the entire boundary (Fig. 3). For each pixel evaluated, the connectivity of the

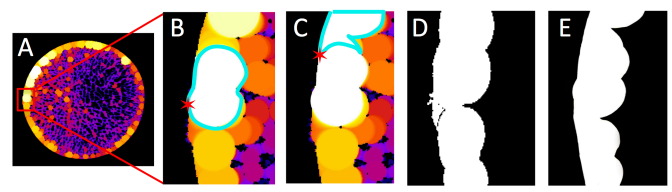


Fig. 3. Using the thickness matrix visualized in (A), the first pixel on the border (red asterisk in B) was identified and a subset of pixels within the set range (teal region) is shown on the thickness image. (C) Consecutive border pixel with corresponding areas. (D) The pixels identified were added to the previous cortical bone image to create a (E) final segmented image.

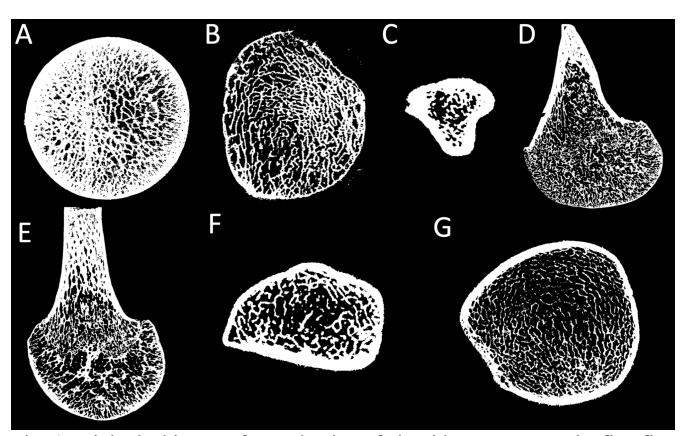


Fig. 4. Biological images for evaluation of algorithm accuracy. The first five data sets are  $\mu$ -CT and the last two data sets are HR-pQCT. (A) Human femoral head and (B) neck, (C) rat tibia, (D) chimpanzee lateral condyle, (E) gorilla lateral condyle, (F) human radius, and (G) human tibia

#### TABLE I

*In vivo* and *ex vivo* data sets evaluated: human femoral head and neck, rat tibia, chimpanzee and gorilla lateral condyles (LC), and human radius and tibia. Listed from higher resolution to lower resolution.

Imaging	Technique	Data Set	Resolution (mm <sup>3</sup> )	Sample Size
μСТ	ex vivo	H. Femur Head	0.05 isotropic	51
	ex vivo	H. Femur Neck	0.05 isotropic	51
	in vivo	Rat Tibia	0.05 isotropic	31
	ex vivo	Chimpanzee LC	$0.05 \times 0.05 \times 1$	41
	ex vivo	Gorilla LC	$0.05 \times 0.05 \times 1$	41
HR-pQCT	ex vivo	H. Radius	0.082 isotropic	51
	in vivo	H. Tibia	0.061 isotropic	51

results was verified to ensure that the pixel of interest was included in each subsequent calculation. If  $th_p=0$ , then no subset of pixels would be identified for segmentation. The resulting subsets were then merged into the final segmented image (Fig. 3D) which was then smoothed by eroding and dilating the image using a disc structural element in combination with a Sovitzky-Golay filter (Fig. 3E).

## D. Evaluation: Biological Images

We evaluated the accuracy of the algorithm on two different imaging modalities: micro-computed tomography ( $\mu$ -CT) and high-resolution peripheral quantitative computed tomography (HR-pQCT). The image sets include four species and three different bones (femur, radius, and tibia)} in order to evaluate the utility of the algorithm across specimens with broad variation in cortical and trabecular thickness (Table I) [27]. Both the rat and human tibia data sets were from in vivo scans and all other data were ex vivo scans. Data from the human proximal femur was aligned to the femoral neck axis after which the femoral head and neck (Fig. 4A, B) were analyzed separately.

As an example of a worst-case scenario, we also evaluated our algorithm on a data set without a closed border, such as the slices found at a mid-slice through the bone. To do so, we ran the algorithm on the mid-section of a lateral condyle from a gorilla  $\mu$ -CT data set (Fig. 4E).

To evaluate speed, the algorithm was tested using a computer with an Intel i3-8109U processor with two cores and four threads available. Users noted their segmentation time for

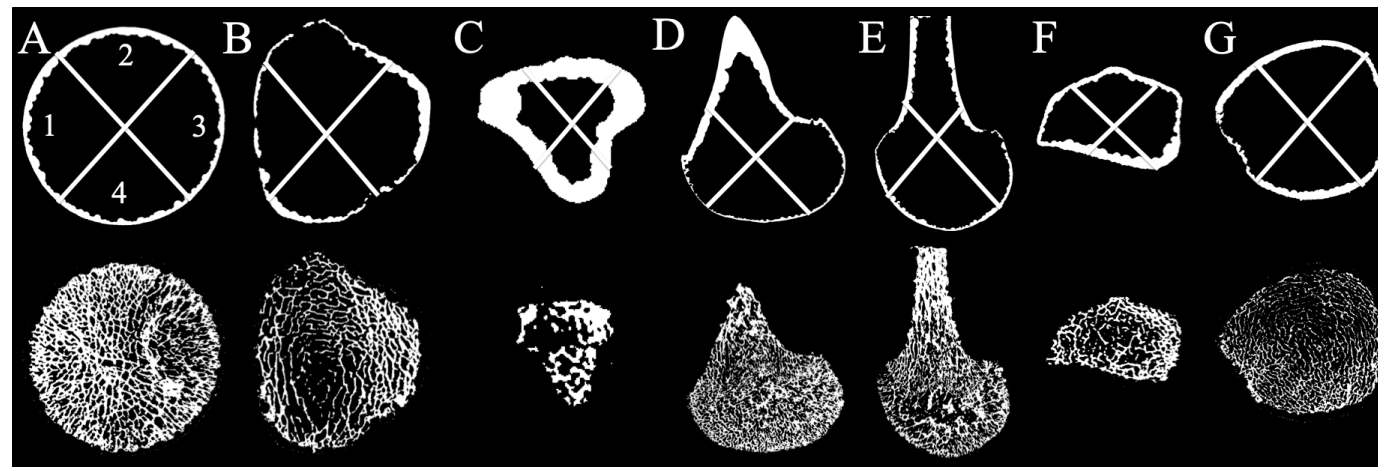


Fig. 5. Resulting cortical and trabecular bone segmentation for (A) human femoral head, (B) femoral neck, (C) rat tibia, (D) chimpanzee lateral condyle, (E) gorilla lateral condyle images, (F) human radius, and (G) human tibia before filtering the  $\mu$ -CT data sets. The human femoral head data set demonstrates how quadrants for all data sets are partitioned and labeled.

comparison to the processing time for the algorithm.

The accuracy of the segmentation was quantified by comparing the results from our algorithm to a "gold standard" segmentation method of hand contouring using Amira (Thermo Fisher Scientific, Waltham, MA, USA). Three experienced users, blinded to the algorithm results, manually segmented 11 regularly-spaced images from each data set. All data was checked for normality using a Kolmogorov-Smirnov test ( $\alpha = 0.05$ ). The median percentage error in cortical area (Ct.Ar) between measurements from our algorithm and manual contouring was calculated. We further subdivided each image into anatomical quadrants, determined the cortical thickness (Ct.Th) for each quadrant, and calculated the median percentage error as compared to the gold standard. Note that the quadrant encompassing the open border for the gorilla data set was not included in the analysis of cortical thickness. Median differences in cortical thickness and percent errors were compared for modality types and within the spatial quadrants. Percentage errors were classified as either Type 1 (over-estimation) or Type II (under-estimation) for Ct.Th. All statistical analyses were performed using RStudio (version 1.1.447, RStudio, Inc).

## III. RESULTS

The algorithm was able to separate trabecular bone from the cortical shell and subchondral compartments in all data sets (Fig. 5). Comparing all data sets (Fig. 6, Supplementary Table I), the median processing time for the algorithm (11.3  $\pm$  10.0 seconds/slice) was approximately 11 times faster than the median time required to manually segment the images (126  $\pm$ 33.2 s/slice). The rat data set took the least amount of time to segment for the algorithm and users ( $\sim 0.42$ ,  $51.7 \pm 27.0$ s/slice). Because of the short time-scale the algorithm used to process the rat tibia data, the average time per slice was estimated and the standard deviation could not be reported. The algorithm took longer to process larger species such as the chimpanzee and gorilla data sets at 30.45 and 29.10 s/slice respectively. This result was reflected in the manual segmentation time, where users took the most amount of time on the chimpanzee data set, 173 s/slice.

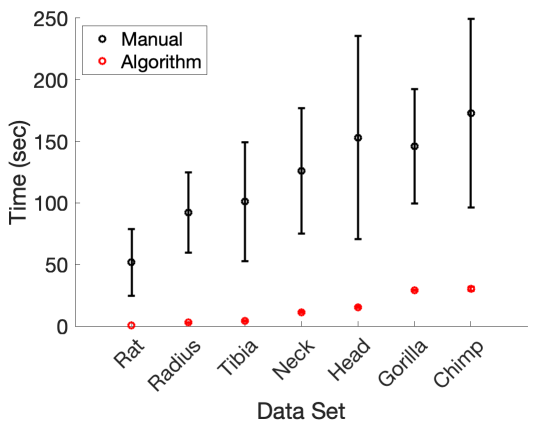


Fig. 6. Algorithm-based and manual segmentation timings for all data sets (average  $\pm$  standard deviation) arranged in order of increasing algorithm-based timing.

Data was not normally distributed; therefore, median ± standard deviations are reported. The algorithm underestimated cortical area for all data sets, yielding a Ct.Ar percentage error of -4.47 ± 4.15 (Supplementary: Fig. 1, Table II). As expected, the largest Ct.Ar percentage error occurred in the  $\mu$ -CT gorilla data set with the open border (- $7.89 \pm 3.83$ ), and the highest accuracy was in the HR-pQCT radius data set (-0.03 ± 1.85). Overall, errors in cortical thickness were less than one voxel and there were more than twice as many Type II errors (n=19, -40.2  $\pm$  71.7  $\mu$ m) than Type I errors (n=8,  $10.5 \pm 31.4 \,\mu\text{m}$ ) (Fig. 7A).

Errors in cortical thickness using  $\mu$ -CT data tended towards underestimation of thickness (Type I error = -36.7  $\pm$  80.2  $\mu$ m) whereas the radius and tibia HR-pQCT data sets slightly overestimated thickness (Type II error = 4.08  $\pm$  77.4  $\mu$ m). In general, the  $\mu$ -CT rat tibia data set demonstrated the highest Ct.Th difference of -58.7  $\pm$  38.8  $\mu$ m (less than a voxel), and the lowest Ct.Th was in the femoral head data (-1.84  $\pm$  37.0  $\mu$ m). There was no significant correlation between cortical thickness and error. The median Ct.Th percent error across all data sets was -2.61  $\pm$  7.75% and was highest in the rat tibia data set (Fig. 7B).

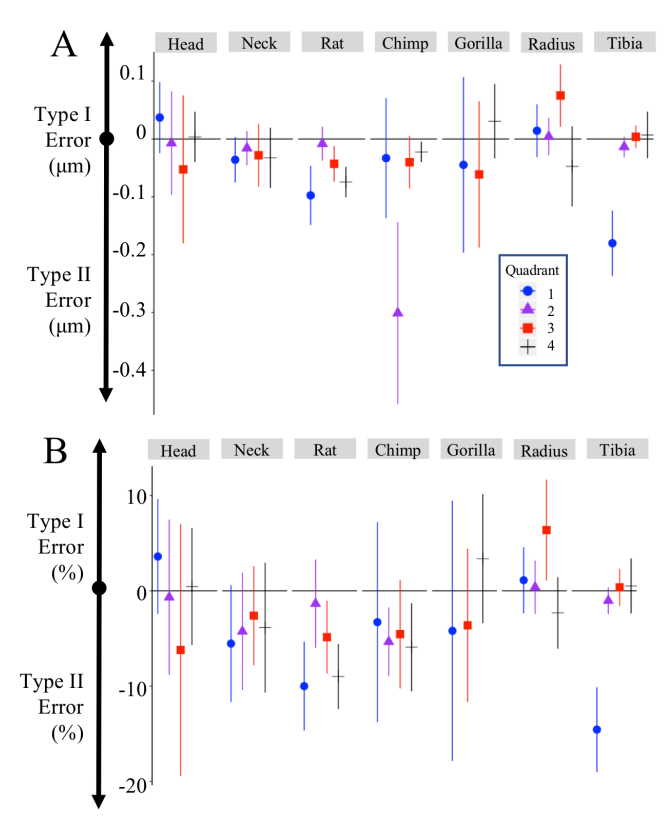


Fig. 7. Distribution of Type I (over-estimation) and Type II (under-estimation) cortical thickness per quadrant displayed in (A) cortical thickness difference and (B) percentage error.

# IV. DISCUSSION

We have presented a structure-based methodology for segmenting cortical or subchondral bone from binarized  $\mu$ -CT and HR-pQCT images. Overall, the thickness results of our algorithm were less than 1 voxel compared to the gold standard resulting in an excellent initial segmentation, but as expected, local thickness measurements were variable between our algorithm and manually derived measurements.

The capacity to identify the cortical and trabecular junction is likely dependent on the variation of cortical thickness within a given image, image resolution, and the degree to which the trabecular bone is connected to the cortical shell. A clear benefit of the algorithm is the consistency in speed with which the cortical boundary could be identified regardless of image complexity. In general, the processing time for both manual and algorithm increased with increasing segmentation area (Supplementary Table I and II). From the rat data with the smallest Ct.Ar to the chimpanzee data with the largest Ct.Ar, the increase in time required to perform the segmentation manually increased from 51.7  $\pm$  27.0 seconds to 173  $\pm$  76.5 seconds (Fig. 6). In comparison, the algorithm time increased from approximately 0.42 seconds to a maximum of 30.5  $\pm$ 1.69 seconds indicating robust performance with respect to segmentation area

There remain options for further decreasing the computational time by parallelizing the processing of data via multiple instances of MATLAB when dealing with large data

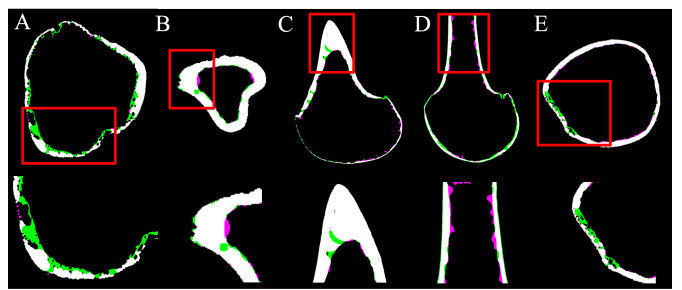


Fig. 8. Examples of type I and II error demonstrated by overlays of manual vs. algorithm segmentation for (A) femoral neck, (B) rat tibia, (C) chimpanzee lateral condyle, (D) gorilla lateral condyle, and (E) human tibia. White displays the regions of overlapping segmentation, magenta displays algorithm segmented bone not present in the manual segmentation (Type I: over-segmentation), green displays manually segmented bone not present in the algorithm segmentation (Type II: under-segmentation).

sets. This option was tested with two instances of MATLAB on the gorilla and chimpanzee data sets and improved the per slice performance by decreasing the time by 60 percent.

The *in vivo* HR-pQCT tibia samples segmentation results were within the same range of error as the *ex vivo* results. The  $\mu$ -CT *in vivo* rat tibia sample resulted in a higher Ct.Ar percentage error (-5.86  $\pm$  2.73 %) compared to the median (-4.46  $\pm$  4.15 %) and had the largest percent error for Ct.Th when analyzing all quadrants together (-6.52  $\pm$  4.72 %). However, caution should be applied in interpreting the percent error values for Ct.Th since large percent errors may be a numerical artifact of the small thickness values (especially for the rat data). On a quadrant basis, Q1 of the HR-pQCT tibia data set demonstrated the highest Type II error (Fig. 7). Estimations for Ct.Th usually differ the most where the cortex is thin [28], but in this case, we believe the users qualitatively over-segmented this quadrant by filling in small gaps and irregularities observable within the cortex (green in Fig. 8E.)

The highest Ct.Ar percentage error (Type II) was in the gorilla data set due to the open border on the 2<sup>nd</sup> quadrant. During manual segmentation, the operator can use their intuition to distinguish between periphery noise and cortical bone, but the algorithm will not segment cortical bone unless it is within the range of thickness values (2). The gorilla data set demonstrated the algorithmic disadvantage with noncontinuous cortical bone, because the algorithm will "assume" the trabecular bone on the open border is cortical bone. However, in practice, this data would be discarded and not included in an analysis of cortical thickness.

The Type II error in the femoral neck was the result of gaps and small convex border sections in the binarized images (displayed in green in Fig. 8A). Fig. 8C demonstrates how pores in the cortical bone can affect the segmentation results. The Type I error (overestimation) in the gorilla condyle was due to inclusion of cortical segments that extended into the trabecular region of bone (magenta regions in Fig. 8D). The circular appearance of these magenta regions is due to the thickness map which is based on the largest inscribed circle at each point in the image. Whereas our final smoothing step removes the majority of these internal circular irregularities, there remains an opportunity for further local refinement

based on user needs.

Others have reported reproducibility errors between different segmentation techniques, [28, 29], but less data is available on comparisons to manual segmentation likely because of its time-consuming nature (Buie et al. conducted manual segmentation). Li et al. used a combination of fuzzy connectivity and topological methods to develop an automated method for segmentation of cortical bone in multi-row detector computed tomography (MDCT) distal tibia samples and cadaveric  $\mu$ -CT ankle samples [16]. Interestingly, they noted that their higher resolution  $\mu$ -CT samples had higher cortical volume percentage errors (11.5%) than their lower resolution MDCT samples (4.9%). Our results followed similar trends when comparing  $\mu$ -CT samples and HR-pQCT samples for both area and thickness in that lower resolution HR-pQCT data resulted in lower errors.

Valentinitsch et al. used a texture-based thresholdindependent segmentation tool (TIST) on the human distal radius of the same resolution as our HR-pQCT radius data set (0.082 isotropic mm<sup>3</sup>) [21]. They also compared their absolute average percentage error Ct.Th results from TIST (10.4 ± 8.0%) to the Scanco standard algorithm (15.5  $\pm$  19.5%) and the segmentation algorithm (9.6  $\pm$  7.7%) from Burghardt et al. [20]. We report the median Ct.Th percentage errors for each quadrant (Fig. 7), but have also analyzed the absolute average percentage error with all quadrants together for comparison. Errors using our structure-based approach were lower 6.25+ 5.44) than the three methods outlined above. Lastly, Kang et al. reported Ct.Th errors within 1-2.5 voxels for the femur using a 3D thresholding based technique. Our median error for the femoral head and neck was less than 0.5 voxels (-22.0  $\pm$ 27.8 µm) [22].

Here we propose that once a binarized image is obtained, the structure itself provides a reliable and unbiased means for separating the cortex from the remaining bone. The results presented were obtained using the same code for all data sets, with Sovitzky-Golay filtering done on the  $\mu$ -CT data. The user inputs that can be changed relate to the border search parameters and the size of the section of image to analyze at one time. These parameters both contribute to the efficiency of the algorithm and can be fine-tuned to increase speed (e.g. minimizing the size of the search window).

An important note is that the algorithm is 2D, with each slice independently processed without input from adjacent slices. The inclusion of three-dimensional thickness information may also improve the accuracy of the algorithm. However, in data sets with changing bone areas, the algorithm in 2D successfully replicated changes in area over the tested range of slices. The accuracy of this algorithm is also dependent on the thresholding process used to remove scanner artifacts and noise. The bone border can be affected by pixel-wide gaps in the bone border and noise artifacts, especially where the border is concave. Problems with removing imaging noise and reading the bone border will cause complications downstream of our process (Fig. 1). Therefore, evaluation of the initial border provides a means of ensuring that a continuous border exists, but the quality of the input binarized

image remains a significant determinant of the resulting morphological measurements.

Our algorithm for separating subchondral and trabecular bone allows for an effective analysis of isolated subchondral and trabecular properties across joint surfaces. This information is useful for a range of questions in comparative biology and clinical applications. For example, the spatial distribution of subchondral density and thickness across joint surfaces has been used to identify normal and pathological patterns of joint loading in human and other mammals [7, 8, 27, 30, 31]. This is also clinically relevant since local (re)modeling responses in subchondral bone may be implicated in osteoarthritis. The body of evidence suggesting that osteoarthritis is a disease that is initiated in subchondral bone is growing. Having the capacity to repeatably identify spatially specific changes in subchondral bone is critical to understanding how subchondral bone serves as an energy absorbing material to dissipate stresses during everyday loading of the joint [8, 31].

We have also shown that this algorithm is effective for regions of diaphyseal bone (radius and tibia) that are used in clinical assessment of bone quality. The use of HRpQCT as a clinical and research assessment tool is increasing and is an inviting imaging modality because of its capacity to image bone microstructure with low radiation. Finally, we have demonstrated utility of our algorithm to assess *in vivo* images of animal skeletal structure. Animal models are among the most widely used pre-clinical methods for evaluating pharmaceutical and exercise interventions targeting bone quality as well as fundamental studies aimed to identify mechanobiological mechanisms driving bone formation, resorption during growth, aging, and in the presence of disease.

# V. CONCLUSION

The assessment of bone microstructure continues to be a critical component to understanding changes in bone during growth, aging, and disease. Our method allows for the quantification of trabecular and cortical structures and properties across joint surfaces with accuracy comparable to other cortical segmentation algorithms based on structure rather than tuned threshold parameters. The median error in cortical area was  $-4.46 \pm 4.15\%$  and the median error in cortical thickness was less than 1 voxel for  $\mu$ -CT data and less than 0.05 voxel for HR-pQCT data. Importantly, this method is implemented using open-source software, ImageJ, and MATLAB which is available in most research laboratories. All code is available for download (https://github.com/TBL-The development of automated UIUC/downloads.git). processing techniques for high-resolution data will allow for more thorough analyses over larger spatial regions and improve full-field characterizations of structure in complex materials.

#### VI. ACKNOWLEDGMENT

We are grateful for the assistance of Sara Moshage,

Hyunggwi Song, Kristian Carlson, Elizabeth Lee, America Guerra, Travis Ross, Iwona Dobrucka, Wawrzyniec Dobrucki, Leo Fabré, VMIL, Harvard Center for Nanoscale Systems, Stuart Warden, and the Beckman Molecular Imaging Lab for their assistance in data collection and processing.

## REFERENCES

- J. D. Currey, Bones: Structure and Mechanics. Princeton, NJ: Princeton University Press, 2002.
- [2] R. Huiskes et al., (2000, June). Effects of mechanical forces on maintenance and adaptation of form in trabecular bone. Nature. 405, pp. 704-706.
- [3] K. J. Carlson et al., (2013, March). Joint Loads in Marsupial Ankles Reflect Habitual Bipedalism versus Quadrupedalism. Public Library of Science (PLoS) ONE. 8(3), pp. e58811
- [4] J. Wolff, The Law of Bone Remodeling (Das Gesetz der Transformation der Knochen). New York, NY: Springer, 1986
- [5] T. L. Kivell, (2016, Feb). A review of trabecular bone functional adaptation: what have we learned from trabecular analyses in extant hominoids and what can we apply to fossils? *Journal of Anatomy*. 228(4), pp. 569-594.
- [6] J. D. Polk et al., (2008, Jul). Knee Posture Predicted from Subchondral Apparent Density in the Distal Femur: An Experimental Validation. The Anatomical Record: Advances in Integrative Anatomy and Evolutionary Biology. 291(3), pp. 293-302.
- [7] A. Su, "The functional morphology of subchondral and trabecular bone in the hominoid tibiotalar joint," Ph.D dissertation, *Dept. Anth., Stony Brook University*, Stony Brook, NY, 2011
- [8] M. Müller-Gerbl et al., (1992, Dec). Demonstration of subchondral bone density patterns by three-dimensional CT osteoabsorptiometry as a noninvasive method for in-vivo assessment of individual long-term stresses in joints. *Journal of Bone and Mineral Research*. 7(S2), pp.
- [9] E. L. Radin et al., (1970, Apr). A comparison of the dynamic force transmitting properties of subchondral bone and articular cartilage. The Journal of Bone and Joint Surgery, 52(3), pp. 444-456
- [10] J. W. Pugh et al., (1974, March). Quantitative studies of human subchondral cancellous bone. The Journal of Bone and Joint Surgery (A). 56(2), pp. 313-321
- [11] T. M. Ryan and R. A. Ketcham, (2002, Aug). Femoral head trabecular bone structure in two omomyid primates. *Journal of Human Evolution*. 43(2), pp. 241-263
- [12] R. J. Fajardo et al., (2007, Apr). Nonhuman anthropoid primate femoral neck trabecular architecture and its relationship to locomotor mode. *The Anatomical Record*. 290(4), pp. 422-436
- [13] T. M. Ryan and A. Walker, (2010, Apr). Trabecular bone structure in the humeral and femoral heads of anthropoid primates. *The Anatomical Record*. 293(4), pp. 719-729
- [14] A. Su et al., (2013, June). Trabecular bone anisotropy and orientation in an Early Pleistocene hominin talus from East Turkana, Kenya. *Journal* of *Human Evolution*. 64(6), pp. 667-677

[15] M. C. Fox et al., (2016, Apr). Reconstructing knee posture in humans, chimpanzees and gorillas: subchondral and trabecular signals. American Association of Physical Anthropologists. 159, pp. 146

- [16] C. Li et al., (2015, Aug). Automated cortical bone segmentation for multirow-detector CT imaging with validation and application to human studies. Medical Physics. 42(8), pp. 4553-4365
- [17] A. K. O. Wang and S. L. Manske, (2018, Apr). A Comparison of Peripheral Imaging Technologies for Bone and Muscle Quantification: A Review of Segmentation Techniques. *Journal of Clinical Densitometry*. pp. 1-16
- [18] T. Gross et al., (2014, Aug). A CT-image-based framework for the holistic analysis of cortical and trabecular bone morphology. Palaeontologia Electronica. 17(3).
- [19] H. R. Buie et al., (2007, Oct). Automatic segmentation of cortical and trabecular compartments based on a dual threshold technique for in-vivo micro-CT bone analysis. Bone. 41(4). pp. 505-515
- [20] A. J. Burghardt et al., (2010, May). Reproducibility of direct quantitative measures of cortical bone microarchitecture of the distal radius and tibia by HR-pQCT. Bone. 47. pp. 519-528
- [21] A. Valentinitsch et al., (2012, June). Automated threshold-independent cortex segmentation by 3D-texture analysis of HR-pQCT scans. Bone. 51, Pp. 480-487
- [22] Y. Kang et al., (2003, May). A new accurate and precise 3-D segmentation method for skeletal structures in volumetric CT data. IEEE: Transactions on Medical Imaging. 22(5). pp. 586-598
- [23] S. Lublinsky et al., (2007, Sept). An Automated Algorithm to Detect the Trabecular-Cortical Bone Interface in Micro-Computed Tomographic Images. Calcified Tissue International. 81(4), pp. 285-293
- [24] D. H. Pahr and P. K Zysset, (2009, Jan). From high-resolution CT data to finite element models: development of an integrated modular framework. Computed Methods in Biomechanics and Biomedical Engineering. 12(1). pp. 45-57
- [25] M. Doube et al., (2010, Sept). BoneJ: free and extensible bone image analysis in ImageJ. Bone. 47(6). pp. 1076-1079
- [26] I. C. Ang et al., "Correlation of Cortical Bone Thickness to Strain in the Proximal Femur Neck," Orthopaedic Research Society Annual Conference, New Orleans, LA, 2018, Poster #1565, Available: https://www.ors.org/Transactions/64/1565.pdf
- [27] K. J. Carlson and B. A. Patel (2006, June). Habitual use of the primate forelimb is reflected in the material properties of subchondral bone in the distal radius. *Journal of Anatomy*. 208(6). pp. 659-670
- [28] G. M. Treece et al., (2010, June). High resolution cortical bone thickness measurement from clinical CT data. Medical Image Analysis. 14. pp. 276-290
- [29] Y. Liu et al., (2014, July). A robust algorithm for thickness computation at low resolution and its application to in vivo trabecular bone CT imaging. IEEE: Transactions on Biomedical Engineering. 61(7). pp. 2057-2069
- [30] H. Pontzer et al., (2006, Jan). Trabecular bone in the bird knee responds with high sensitivity to changes in load orientation. The Journal of Experimental Biology. 209(Pt. 1). pp. 57-65
- [31] H. Madry et al. (2010, Jan). The basic science of the subchondral bone. Knee Surgery, Sports Traumatology, Arthroscopy. 18(4). pp. 419-433